

Guided-Wave-Excited Binary Huygens' Metasurfaces for Dynamic Radiated-Beam Shaping with Independent Gain and Scan-Angle Control

Minseok Kim[✉] and George V. Eleftheriades^{*}

The Edward S. Rogers Department of Electrical and Computer Engineering, University of Toronto, Toronto, Canada



(Received 9 December 2020; revised 29 March 2021; accepted 16 April 2021; published 17 May 2021)

This paper presents a reconfigurable metasurface that is able to dynamically and independently control the gain and propagation direction of the radiated field, with reduced biasing complexity and power consumption at a low profile. Moreover, the proposed metasurface is guided-wave fed thus leading to a compact tunable leaky-waveguide structure. Heretofore, reported reconfigurable metasurfaces have mainly demonstrated dynamic tailoring of free-space waves by redistributing their reflection or transmission phase profiles at a fixed amplitude. In contrast, we demonstrate dynamic transformation of a guided wave into an aperture field with controlled amplitude such that the gain and scan angle of the corresponding radiated field are dynamically and independently controlled. In particular, the aperture field is digitally synthesized by the proposed tunable Huygens' metasurface whose local transmission coefficient is able to be dynamically tuned as two digital bits of $-|T_o|$ and $+|T_o|$, where T_o represents a user-defined constant. This digital synthesis and the deliberate utilization of a nonbianisotropic type Huygens' metasurface simplify biasing requirements, and make the proposed design more feasible. Through simulations and experiments, we show dynamic steering of a beam from -40° to $+40^\circ$, and two broadside radiations with different radiation gains at a fixed operating frequency of 5 GHz.

DOI: [10.1103/PhysRevApplied.15.054037](https://doi.org/10.1103/PhysRevApplied.15.054037)

I. INTRODUCTION

The idea of arbitrary shaping of electromagnetic (EM) waves with low-profile structures has triggered rapid development in the field of artificial EM surfaces (i.e., metasurfaces) and opened up exciting opportunities in EM and photonic research. These surfaces comprise subwavelength-sized “meta-atoms” which locally interact with an incident EM wave and introduce abrupt field discontinuities to produce a desired radiation. By engineering the structural properties of the meta-atoms, various field manipulations have been demonstrated such as light bending [1–6], cloaking [7–9], and holograms [10–12]. In particular, the introduction of Huygens' metasurfaces (HMSs) has enabled unprecedented control over EM waves through explicit utilization of both electric and magnetic responses of their meta-atoms [5,6,13–16]. These Huygens' meta-atoms induce suitable electric and magnetic surface currents that are deduced from the Schelkunoff's equivalence principle such that the pertinent boundary conditions are satisfied for a certain desired field distribution [17]. Based on this principle, HMSs have been demonstrated to manipulate various aspects of EM waves such as their amplitude, phase, and polarization [13–16,18,19]. Despite such unique field manipulation capabilities, however, most of

their realizations to date have been based on static meta-atoms. As a result, their wave-control capabilities have been inherently limited to the geometrical parameters of the constituent meta-atoms.

On the other hand, to further extend the practical applicability of metasurfaces especially in the areas of high-rate communications (e.g., Internet-of-Things, 5G, and 6G), much of the recent effort has been devoted to the realization of *reconfigurable* microwave metasurfaces for dynamic shaping of radio-frequency waves [20–41]. In particular, to achieve dynamic wavefront control based on a compact form factor, there has been considerable effort in directly integrating these reconfigurable metasurfaces within wave-guiding structures. In this effort, reconfigurable leaky-wave antennas (LWAs) that incorporate various kinds of *guided-wave-excited* tunable metasurfaces have been proposed, which utilize active lumped elements [42–45] and phase-transition materials (e.g., liquid crystals [46,47]) in their reconfigurable meta-atom designs to attain the necessary tunability. Instead of manipulating free-space waves, which requires an external source to be placed sufficiently far away from the surfaces, these guided-wave-excited tunable metasurfaces transform a confined mode (i.e., a guided mode) into a certain desired radiation, and dynamically tailor its shape by altering their surface properties (e.g., the local transmission phases and surface impedances). For example, LWAs

^{*}gelefth@ece.utoronto.ca

based on tunable composite right- and left-handed meta-atoms have been demonstrated to dynamically steer a beam at a fixed operating frequency [46]. By balancing the resonance frequencies of the series and shunt branches of their meta-atoms, these LWAs have overcome the limitations imposed by the open-stopband effect and demonstrated steering of a beam through broadside. On the other hand, guided-wave-excited surfaces that dynamically modulate the phase of the transmitted field have also been demonstrated based on an antenna-filter-antenna architecture, which utilizes an array of receiving and transmitting antennas with reconfigurable filters inserted in between [48]. In addition, period-reconfigurable LWAs that incorporate certain switching mechanisms have also been extensively investigated [42,43]. In these surfaces, the periodicity of meta-atoms with “ON” and “OFF” status is dynamically altered to control the phase constant of the corresponding n th space harmonic that gets coupled to the radiated field, thereby dynamically steering a beam.

Although these demonstrations represent the culmination of impressive theory and fabrication, they yet provide limited tunability in the sense that they only achieve dynamic wavefront shaping at a fixed transmission amplitude of their guided-wave-excited metasurfaces. As such, they do not provide any means to also dynamically and independently control the *gain* of a LWA (which is related to the amplitude of the radiated field), although such an ability is highly desirable in achieving complete wave-control capabilities. To also independently control the gain, the integration of a reconfigurable HMS with a LWA can be considered, as the static HMSs have been demonstrated to arbitrarily and independently control the amplitude and phase of the scattered field [13,49,50]. Nevertheless, the realization of a reconfigurable HMS is particularly challenging owing to the difficulties in locally tuning both electric and magnetic responses of individual meta-atoms and designing a biasing circuitry that would not degrade the wave-control performance of the metasurface. As such, only a few reconfigurable HMSs have been reported to date [51,52]. Moreover, owing to the aforementioned difficulties, they have also merely focused on dynamically shaping EM waves at a fixed transmission amplitude only for free-space waves. Recently, however, Kim *et al.* have proposed a reconfigurable omega-bianisotropic HMS that can be integrated with a LWA to independently control the gain and the angular direction of the radiated field [53]. However, its physical realization was hindered owing to the complex biasing requirements and, as a consequence, only the numerical demonstration was provided. As such, there is still an absence of an ultimate reconfigurable LWA that is able to (i) continuously scan over a wide angular range including broadside and (ii) independently control the amplitude of the radiated field at a fixed operating frequency.

In this work, we aim to fill this void by proposing a viable route toward dynamic and independent control of the gain and the scan angle of a reconfigurable LWA. Specifically, we achieve this by integrating a guided-wave-excited tunable binary HMS with a LWA to (i) arbitrarily steer the radiated field over a wide angular range including broadside, while (ii) dynamically controlling the local amplitude of the corresponding aperture field at a fixed operating frequency of 5 GHz. The preliminary numerical results were reported in [54], however this work presents the detailed theoretical background and the experimental demonstrations. In particular, to address the first milestone, we consider dynamically transforming a guided mode into an aperture field, which would propagate to a desired radiation in the far-field zone. Specifically, we leverage the theory of Fourier optics to obtain suitable aperture fields to steer a beam from -40° to $+40^\circ$. On the other hand, to control the amplitude of the radiated fields, the aperture fields are digitally synthesized with controlled amplitude via the proposed tunable binary HMS. We show that the local transmission coefficients of the proposed HMS can be individually tuned to be either $+T_o$ or $-T_o$ where T_o is a user-defined constant that governs the local radiation amplitude. On the other hand, the local reflection phases are maintained at 180° regardless of the choice of T_o to support a guided mode. It should be highlighted that the proposed binary HMS is of a nonbianisotropic type (i.e., there is no magnetoelectric coupling coefficient), yet these scattering properties are realized without violating the passivity and losslessness conditions. In particular, the proposed HMS is physically realized by symmetrically cascading three tunable admittance layers each comprising an array of dual-loop meta-atoms. By applying suitable bias voltages to the dual-loop meta-atoms that contain varactor diodes, particular surface admittance values are encoded to synthesize the desired binary states with user-defined T_o for the cascaded structure. As it shall be shown, this digital sampling of the aperture field allows the meta-atoms to bypass fully covering 360° of transmission phase tunability (thereby alleviating the biasing complexity), and yet allows steering of a beam over a wide angular range. Finally, we show how the proposed HMS can be integrated within a wave-guiding structure to form a compact and versatile wave-control system, and experimentally verify the fabricated waveguide based on far-field anechoic chamber measurements.

II. THEORY AND CONCEPT

A. Fourier-perspective beam steering

The objective of this work is to realize a compact and versatile wave-control system that can (i) arbitrarily steer the radiated field over a wide angular range, while (ii) dynamically controlling the amplitude of the radiated field at the operating frequency of 5 GHz. For this purpose, we

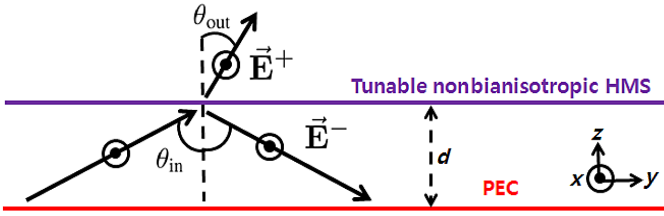


FIG. 1. A schematic of the proposed reconfigurable LWA that utilizes a guided-wave-excited tunable HMS.

envision a reconfigurable LWA structure in which the top PEC plate of a parallel plate waveguide is replaced by a tunable nonbianisotropic HMS as shown in Fig. 1. Here, the role of our nonbianisotropic HMS is to transform a guided mode into an aperture field which would propagate to a desired radiation in the far-field zone. Specifically, to obtain such an aperture field, we invoke the theory of Fourier optics which states that an aperture field and the corresponding Fraunhofer radiation form a Fourier transform pair. In light of this theory, our tunable HMS aims to dynamically synthesize various aperture fields, \vec{E}_{ap} , such that the resulting radiated field can also be dynamically manipulated at will. In particular, to dynamically steer a beam, we require the HMS to synthesize an aperture field in the form given as

$$\vec{E}_{\text{ap}} \propto \cos \left[\left(\beta_y^- - \beta_y^+ \right) y \right] e^{j\xi} e^{-j\beta_y^- y} \vec{a}_x, \quad (1)$$

where ξ represents a constant phase shift that can be added to the wave as a degree of freedom, and β_y^- and β_y^+ denote the y -components of the phase constants of the guided mode and the desired radiation, respectively. These phase constants in (1) can be related to the angle of incidence inside the waveguide, θ_{in} , and the desired radiation angle, θ_{out} , as

$$\beta_y^- \simeq k_o \sin(\theta_{\text{in}}) \quad (2a)$$

$$\beta_y^+ \simeq k_o \sin(\theta_{\text{out}}), \quad (2b)$$

where k_o is the free-space wavenumber. In particular, the angle of incidence can further be expressed in terms of the waveguide dimensions by requiring that the guided mode resembles the TE_{10} mode as

$$\theta_{\text{in}} \simeq \sin^{-1} \left[\sqrt{k_o^2 - (\pi^2/d^2)/k_o} \right], \quad (3)$$

where d represents the thickness of the waveguide.

To illustrate how the aperture field in (1) would result in the desired radiation, we judiciously choose θ_{in} and θ_{out} such that there is only one of the Fourier components of (1) residing within the visible region (i.e., the spatial frequency range within $\pm k_o$). For example, Fig. 2(a) shows

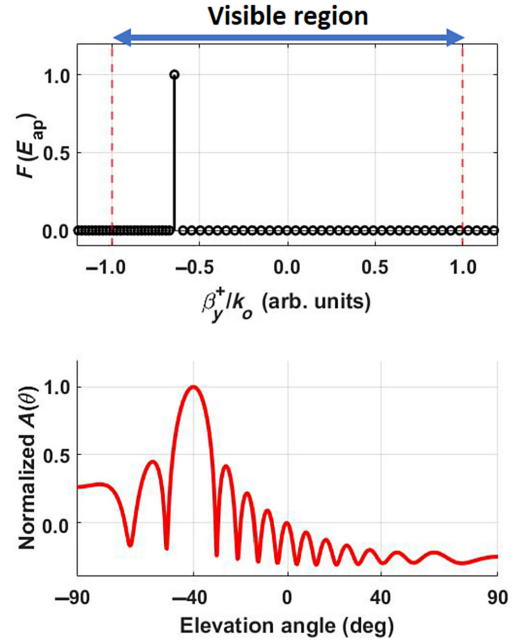


FIG. 2. (a) The spectrum of (1) in the case of $\theta_{\text{in}} = 54^\circ$ and $\theta_{\text{out}} = -40^\circ$ illustrating that there is only one propagating mode inside the visible region and (b) the corresponding array factor with $\Delta y = \lambda/4$ and $N = 28$.

the spatial spectrum of (1) in which θ_{in} and θ_{out} are set to 54° and -40° , respectively. As seen, only one Fourier component remains inside the visible region, which translates to a propagating mode, and the other conjugate Fourier component is pushed to the “invisible” region. In addition, the radiation pattern from the aperture field can also be estimated by utilizing the antenna-array analysis. In this analysis, the aperture field given in (1) is evaluated at $y = n\Delta y$ (where n denotes an index and Δy is a sampling interval), and the evaluated values, I_n , are treated as the weights of the isotropic sources that are located at $y = n\Delta y$. The array factor, A , can then be calculated as

$$A(\theta) = \sum_{n=0}^{N-1} I_n e^{jk_o \sin(\theta) n \Delta y}. \quad (4)$$

Figure 2(b) shows the magnitude of the resulting array factor in decibels for $\theta_{\text{in}} = 54^\circ$ and $\theta_{\text{out}} = -40^\circ$. In accordance with the Fourier analysis, a main beam is seen at the prescribed output angle of $\theta_{\text{out}} = -40^\circ$. Based on this Fourier optics perspective, we demonstrate dynamic steering of a beam from $\theta_{\text{out}} = -40^\circ$ to $\theta_{\text{out}} = +40^\circ$ including broadside. In particular, throughout the paper, the incident angle of 54° will be assumed which corresponds to the waveguide thickness of 0.85λ according to (3).

Although the discussion thus far has concerned the general idea behind controlling the direction of the radiated field, we have not yet shown how the amplitude of the field can also be independently controlled. For this purpose, the

following discussion considers the realization of a tunable HMS that can synthesize the desired aperture field with controlled amplitude.

B. Synthesis of an aperture field with controlled amplitude

Whereas the previous discussion concerned the general idea behind dynamic beam shaping from the perspective of Fourier optics, we now consider dynamic and independent amplitude control for the radiated field. To this end, we aim to dynamically control the amplitude of the aperture field (which is directly related to that of the radiated field), by utilizing a tunable HMS. Specifically, the proposed tunable HMS consists of three cascaded reconfigurable admittance layers that are separated by $t \ll \lambda$ as schematically shown in Fig. 3. Here, we envision dynamically tuning the surface admittance profiles in each layer (i.e., Y_1 and Y_2) such that the corresponding reflection and transmission properties of the cascaded structure are independently controlled to (i) support a guided mode and (ii) transform the guided mode into a desired aperture field with controlled amplitude. For the proposed structure, the first and the third admittance layers are assumed to be identical (i.e., the structure is symmetric), which implies that the tunable HMS is of a nonbianisotropic type. It should be noted that an asymmetric structure would result in an omega-bianisotropic HMS which, in theory, can offer more advanced wave-control capabilities. However, such an advantage comes at the cost of complicated biasing requirements because the asymmetry also implies that all layers would have to be differently biased or tuned. In addition, although it has been theoretically proven that three admittance layers are sufficient and necessary to realize any type of HMSs [55], it usually takes at least four layers to realize an omega-bianisotropic HMS in practice, mostly due to the Ohmic losses, which further complicates the biasing of individual layers [47,53,56]. To alleviate such biasing complexity, we deliberately utilize a nonbianisotropic HMS for which the first and the third admittance layers can share the same biasing network. Although a single tunable admittance layer would further alleviate the biasing complexity, a single layer which only provides an electric response is not sufficient to independently and arbitrarily control the transmission and reflection properties. As such, three tunable admittance layers are hereby considered to independently and dynamically control the reflection and transmission characteristics of the HMS, thereby simultaneously synthesizing the desired guided mode and the aperture field.

To relate the required scattering properties of the proposed HMS with the desired guided mode and the aperture field, we first stipulate the local fields at $z = 0^\pm$ as (referring to Fig. 3),

$$\vec{E}_{\text{inc}} = E_{i0} \vec{a}_x e^{-jk_o \sin(\theta_{\text{in}})y}, \quad (5a)$$

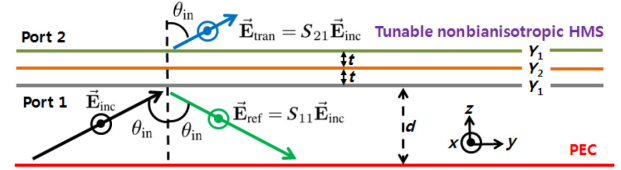


FIG. 3. The three cascaded reconfigurable admittance layers that form the tunable HMS, and the local field distribution at $z = 0^\pm$. It is assumed that the three-layered HMS is infinitesimally thin and it is located at $z = 0$.

$$\vec{E}_{\text{trans}} = S_{21} E_{i0} \vec{a}_x e^{-jk_o \sin(\theta_{\text{in}})y}, \quad (5b)$$

$$\vec{E}_{\text{ref}} = S_{11} E_{i0} \vec{a}_x e^{-jk_o \sin(\theta_{\text{in}})y}, \quad (5c)$$

where S_{21} and S_{11} represent the transmission and the reflection profiles of the proposed HMS (i.e., the cascaded structure), respectively, and the subscripts 1 and 2 refer to ports 1 and 2 of the HMS, respectively (Fig. 3). Here, S_{21} is stipulated as

$$S_{21} = |T_o| \cos \left[\left(\beta_y^- - \beta_y^+ \right) y \right] e^{j\xi}, \quad (6)$$

such that the guided mode would get transmitted as the desired aperture field in the form given in (1) along the surface. In particular, to also control the amplitude of the aperture field, a user-defined amplitude, $|T_o|$, is included in (6). It should be highlighted that this user-defined amplitude can take a nonuniform form in which case a certain amplitude tapering can also be applied along the metasurface. Furthermore, it should be also mentioned that the transmission profile given in (6) can also be derived from the perspective of the theory of holography. Specifically, by treating the guided mode as the reference wave and the desired radiation as the objective wave, it can be shown that the corresponding holographic pattern results in the form given in (6). On the other hand, the reflection profile, S_{11} , of the tunable HMS is defined as

$$S_{11} = \sqrt{1 - |S_{21}(y)|^2} e^{\pm j\pi}, \quad (7)$$

such that the reflection phase of the HMS is maintained at 180° regardless of the choice of S_{21} to support a TE₁₀-like mode inside the waveguide. In addition, the reflection magnitude is set to $\sqrt{1 - |S_{21}(y)|^2}$ to satisfy the local power conservation condition. At this point, it should be recalled that (6) and (7) are defined based on the local fields that are present just below and above the HMS (i.e., \vec{E}_{inc} , \vec{E}_{ref} , and \vec{E}_{tran} in Fig. 3) which all propagate at the angle of incidence, θ_{in} . This, however, does not imply that the radiation from the proposed waveguide is fixed to θ_{in} . Although the local transmitted fields may indeed propagate at θ_{in} , we also modulate these fields in the form given in (1) such

that they would constructively interfere at a certain desired radiation angle, θ_{out} .

The discussion thus far has established the desired transmission and reflection profiles along the tunable HMS to dynamically synthesize various aperture fields with controlled amplitude, while supporting a guided mode. However, we have not yet specified the required surface admittance values in each layer that would cascade to result in the desired scattering parameters in (6) and (7). To obtain these values, the local field quantities in (5) are related to the constitutive parameters of the HMS in the form of the electric impedance (Z_{se}) and the magnetic admittance (Y_{sm}). Specifically, the nonbianisotropic boundary

conditions are given by [57,58],

$$\frac{1}{2} (\vec{\mathbf{E}}_{\text{inc}} + \vec{\mathbf{E}}_{\text{ref}} + \vec{\mathbf{E}}_{\text{trans}}) = Z_{\text{se}} \left\{ \vec{\mathbf{a}}_z \times [\vec{\mathbf{H}}_{\text{trans}} - (\vec{\mathbf{H}}_{\text{inc}} + \vec{\mathbf{H}}_{\text{ref}})] \right\} \quad (8a)$$

$$\frac{1}{2} (\vec{\mathbf{H}}_{\text{inc}} + \vec{\mathbf{H}}_{\text{ref}} + \vec{\mathbf{H}}_{\text{trans}}) = Y_{\text{sm}} \left\{ -\vec{\mathbf{a}}_z \times [\vec{\mathbf{E}}_{\text{trans}} - (\vec{\mathbf{E}}_{\text{inc}} + \vec{\mathbf{E}}_{\text{ref}})] \right\}, \quad (8b)$$

from which the required constitutive parameters, Z_{se} and Y_{sm} , can be expressed in terms of the local field quantities as

$$Z_{\text{se}} = \frac{E_{\text{inc}} + E_{\text{ref}} + E_{\text{trans}}}{2(H_{\text{inc}} + H_{\text{ref}} - H_{\text{trans}})}, \quad (9a)$$

$$Y_{\text{sm}} = \frac{H_{\text{inc}} + H_{\text{ref}} + H_{\text{trans}}}{2(E_{\text{inc}} + E_{\text{ref}} - E_{\text{trans}})}. \quad (9b)$$

These constitutive parameters can further be related to the surface admittance values in each layer by modeling the cascaded structure as the transverse equivalent network (TEN) as shown in Fig. 4 [4]. In this modeling, each admittance layer is considered as a shunt network, and the gaps between the layers are modeled as transmission-line segments having a characteristic impedance of $\eta_o / \cos(\theta_{\text{in}})$. Hereafter, the gap distance, t , is assumed as $\lambda/6$ (10 mm). Based on the TEN model, the relationship between the constitutive parameters and the surface admittance profiles can be analytically calculated as [59]

$$Y_1 = \frac{j \Delta Z \cos[k_o \cos(\theta_{\text{in}})t] + [\eta_o / \cos(\theta_{\text{in}})](Z_{22} + Z_{12}) \sin[k_o \cos(\theta_{\text{in}})t]}{[\eta_o / \cos(\theta_{\text{in}})] \Delta Z \sin[k_o \cos(\theta_{\text{in}})t]}, \quad (10a)$$

$$Y_2 = \frac{2 \Delta Z - j 2[\eta_o / \cos(\theta_{\text{in}})] Z_{12} \sin[2k_o \cos(\theta_{\text{in}})t]}{[\eta_o / \cos(\theta_{\text{in}})]^2 Z_{12} \{\cos[2k_o \cos(\theta_{\text{in}})t] - 1\}}, \quad (10b)$$

where ΔZ is the determinant of the impedance matrix that models the equivalent circuit of the Huygens' meta-atom (i.e., a lattice network) [60], and Z_{ij} is the corresponding impedance parameters. In particular, these impedance parameters are given as [60],

$$Z_{11} = Z_{22} = Z_{\text{se}} + 1/4Y_{\text{sm}}, \quad (11a)$$

$$Z_{12} = Z_{21} = Z_{\text{se}} - 1/4Y_{\text{sm}}. \quad (11b)$$

From (10) and (11), the required surface admittance profiles can then be obtained for the desired scattering parameters in (6) and (7). This also implies that the radiation angle, θ_{out} , and the amplitude of the radiated field (which is related to $|S_{21}|$, or equivalently $|\vec{\mathbf{E}}_{\text{ap}}|$), can be dynamically and independently controlled, provided that Y_1 and Y_2 are suitably tuned. In this work, we utilize this idea of dynamic tuning of Y_1 and Y_2 to dynamically and

independently control the radiation angle and the amplitude of the radiated field. However, because the utilized HMS is of a nonbianisotropic type, the passivity and losslessness conditions are not guaranteed to be satisfied for an arbitrary set of S_{21} and S_{11} . Indeed, this is a well-known problem of a nonbianisotropic HMS, and the investigation of the nonbianisotropic boundary conditions in (8) uncovers the origin of the issue. Specifically, in (8), there are two sets of complex unknowns (Z_{se} and Y_{sm}) and two sets of complex equations, which inevitably result in unique solutions of Z_{se} and Y_{sm} for any desired sets of S_{21} and S_{11} (see [16]). As such, the real parts of Z_{se} and Y_{sm} can be nonzero or negative values in some regions along the surface even if $|S_{11}|^2 + |S_{21}|^2 = 1$. This implies that the admittance layers must inject or absorb power in those regions to synthesize the desired scattering parameters, which is not a trivial task. To overcome this issue, we judiciously choose the phase of S_{21} [i.e., ξ in (6)] to be

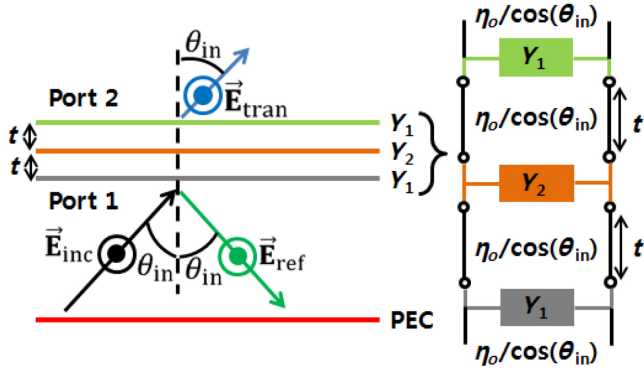


FIG. 4. The transverse equivalent network model of the three-layered HMS. η_o represents the free-space characteristic impedance.

$\pm 90^\circ$ such that Y_1 and Y_2 remain purely imaginary (see Appendix A). Specifically, Fig. 5(a) shows $\text{Re}(1/Y_1)$ and $\text{Re}(1/Y_2)$ for S_{21} with $\xi = \pm 90^\circ$ and various T_o . Here, the surface impedance values are shown merely for better visibility, and θ_{out} is again assumed to be -40° for a demonstration purpose, but it can be readily shown that other angles result in the same trend as in Fig. 5(a) (i.e., zero surface resistances). As seen in Fig. 5(a), $\text{Re}(1/Y_{1,2})$ is exactly zero for the desired S_{21} and S_{11} with various T_o , which indicates that the proposed nonbianisotropic HMS synthesizes the desired scattering parameters without violating the passivity and losslessness conditions.

On the other hand, Fig. 5(b) shows that dynamically altering the scattering properties requires the ability to dynamically and arbitrarily synthesize various surface reactance values [i.e., $\text{Im}(1/Y_{1,2})$] along the admittance layers. This imposes a rather challenging biasing requirement as every meta-atom that comprises the surface admittance layers would need to be individually biased at various levels. Although the first and the third layers would share the same biasing for our nonbianisotropic HMS, we aim to further alleviate such a complicated biasing requirement through digitally sampling the required scattering parameters. Indeed, the fact that our nonbianisotropic HMS satisfies the passivity and losslessness conditions for $\xi = \pm 90^\circ$ is well suited for such a purpose. Specifically, it is noted that any sets of S_{21} with $\xi = -90^\circ$ and $\xi = +90^\circ$ has a phase difference of 180° , hence two binary bits of “ $-|T_o|$ ” and “ $+|T_o|$ ” can be utilized to digitally sample the desired scattering parameters. In sampling S_{21} with these two digital bits, we have also chosen a certain phase threshold, Φ_{th} , such that if the magnitude of the cosine argument of S_{21} in (6) is less than Φ_{th} [i.e., $|\left(\beta_y^- - \beta_y^+\right)y_n| < \Phi_{\text{th}}$], then the value of S_{21} at $y = y_n$ is set to $|T_o|e^{+j\pi/2}$. On the other hand, if the magnitude of the cosine argument is greater than Φ_{th} , then S_{21} at $y = y_n$ is set to $|T_o|e^{-j\pi/2}$ [12,61]. As an illustration, the solid black

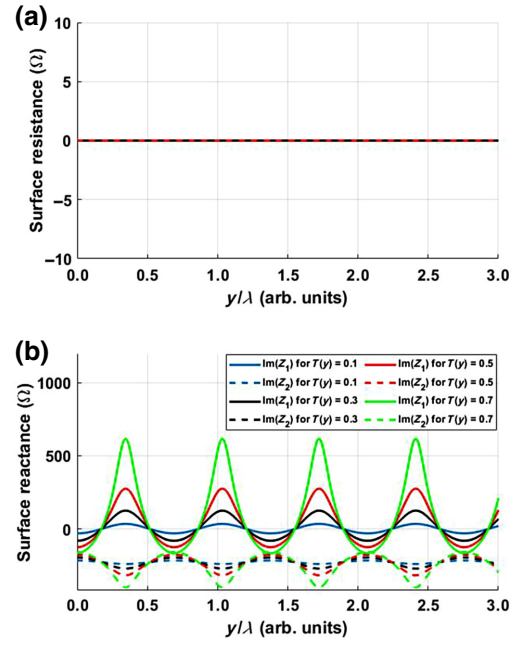


FIG. 5. (a) The real and (b) imaginary parts of $1/Y_{1,2}$ for S_{21} with various T_o and $\xi = \pm 90^\circ$.

curve in Fig. 6(a) shows the required $\text{Im}[S_{21}]$ distribution for $\theta_{\text{in}} = 54^\circ$, $\theta_{\text{out}} = -40^\circ$, $T_o = 0.3$, and $\xi = \pm 90^\circ$, whereas the red dotted curve shows the digitally sampled $\text{Im}[S_{21}]$ distribution with $\Phi_{\text{th}} = 97.5^\circ$. It should be noted that this digital sampling can result in higher-order space harmonics which may contribute to unwanted radiations. However, the phase threshold, Φ_{th} , can be utilized as a design parameter to fine-tune a desired radiation in full-wave simulations, which we discuss in the following section. For example, Fig. 6(b) compares two array factors [see (4)] that are obtained from the ideal transmission profile [i.e., the black curve in Fig. 6(a)] and the digitally sampled distribution [i.e., the red curve in Fig. 6(a)]. In this calculation, the length of the HMS is assumed to be 7λ -long, and $\lambda/4$ is again chosen as the sampling interval (i.e., Δy). Owing to the digitization, the sidelobe level is increased. However, the peak value is well maintained at the prescribed scan angle of -40° , and we do not observe a drop in the peak value. Indeed the peak value is increased for the digitized S_{21} distribution, which can be understood from Fig. 6(a). Specifically, it is seen that the magnitude of S_{21} continuously varies from 0 to 0.3 for an ideal S_{21} distribution, whereas that of the digitized S_{21} distribution is maintained at 0.3. As such, the average transmission along the waveguide is higher for the digitized distribution which would lead to a higher gain value.

Finally, to briefly sum up the proposed idea of dynamic steering of the radiated field and independent amplitude control of the field, Fig. 6(c) shows the antenna-array

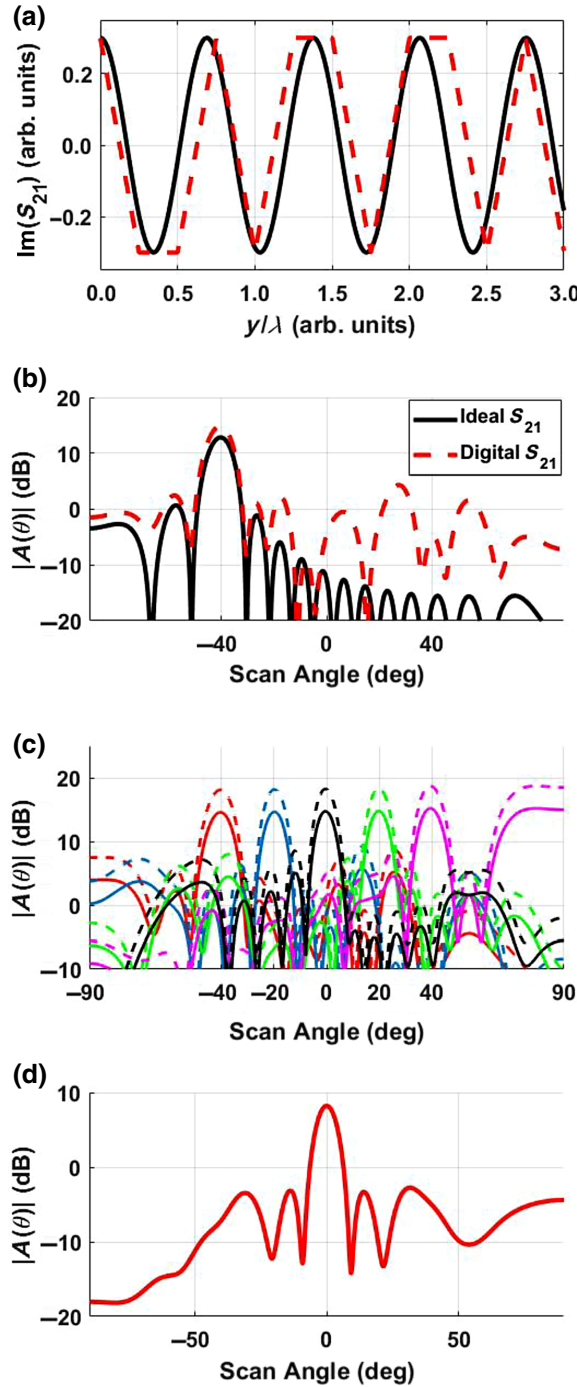


FIG. 6. (a) The ideal (solid) and digitally sampled (dotted) distribution of $\text{Im}[S_{21}]$ and (b) the corresponding array factors with $\Delta y = \lambda/4$. (c) The array factors of the digitally synthesized $\text{Im}[S_{21}]$ at various scan angles with $T_o = 0.3$ (solid) and $T_o = 0.45$ (dotted). (d) The array factor of the digitally synthesized $\text{Im}[S_{21}]$ with a nonuniform distribution of T_o that synthesizes a broadside Dolph-Chebyshev antenna array with a sidelobe level of 10 dB.

analysis results for the digitally sampled S_{21} with various θ_{out} and T_o . In particular, the solid curves in Fig. 6(c) correspond to the array factors with $T_o = 0.3$, and

the dotted curves correspond to those with $T_o = 0.45$. Figure 6(c) shows that the maximum values for each main beam are increased by approximately 3.5 dB by increasing T_o from 0.3 to 0.45. At this point, it should be reiterated that the user-defined amplitude, T_o , can be a nonuniform function of z as the proposed HMS can *locally* synthesize any values of S_{21} without violating the passivity and losslessness conditions. For example, T_o can be defined as $e^{\alpha z}$ to counter the radiation loss that is related to the leakage constant, α , of a leaky waveguide. In addition, T_o can also be designed to synthesize various antenna-array weights to realize complex far-field patterns. For example, Fig. 6(d) shows the case where T_o is configured to synthesize a Dolph-Chebyshev antenna array for broadside radiation with a prescribed sidelobe level of -10 dB. As shown, nearly equal sidelobes can be observed, which is the unique feature of a Dolph-Chebyshev pattern, and the sidelobe level is -10.96 dB which is close to the prescribed one. Synthesizing a nonuniform T_o , however, would require different biasing for each of the meta-atoms. To simplify the following numerical and experimental demonstrations and as a proof of concept, we shall demonstrate the case where all of the meta-atoms are configured to a variable constant, T_o , thereby demonstrating independent gain control. Nevertheless, even this seemingly simple example of amplitude tuning cannot be achieved with previous tunable surfaces that only offer phase control. Indeed, for phase-only tunable metasurfaces, the effect of changing T_o can only be achieved by physically changing their surface dimensions, or by cascading two of these surfaces (as has been done with static surfaces in [50]), which would significantly complicate their biasing. In what follows, we propose a meta-atom design whose reactance (or susceptance) values can be electronically tuned to physically synthesize the desired impedance profiles such as that shown in Fig. 5.

III. PHYSICAL REALIZATION AND FULL-WAVE VERIFICATION

A. Reconfigurable meta-atom and the integration to a waveguide

Whereas the previous section has established the relationship between the desired scattering properties and the surface admittance profiles, this section discusses the physical realization of tunable admittance layers that can dynamically synthesize various admittance profiles. To this end, we propose double metallic (copper) loops with a varactor diode as a reconfigurable meta-atom to form the tunable admittance layers. The dual-loop topology has been previously utilized in various metasurfaces and frequency selective surfaces, and its EM response has been studied extensively in terms of its equivalent circuit model (two series LC networks in parallel) [62]. The schematics of the proposed meta-atom are shown in Figs. 7(a)

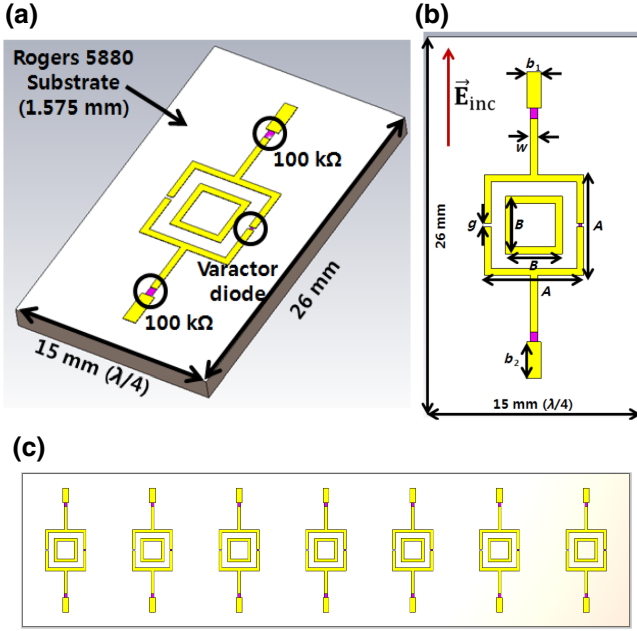


FIG. 7. (a),(b) Schematics of the proposed reconfigurable dual-loop meta-atom and (c) an array of the meta-atoms forming the tunable admittance layer.

and 7(b), and an array of these meta-atoms that forms the proposed tunable admittance layer is shown in Fig. 7(c). Here, the meta-atom periodicity is set to 15 mm ($\lambda/4$) and the metallic loops are printed on 1.575-mm-thick Rogers 5880 substrates. It is noted that the periodicity is deliberately set to be slightly larger than typical meta-atoms in order to minimize the usage of the varactor diodes. On the right-hand side of the outermost loop, a varactor diode from MACOM (MAVR-000120-1141) is integrated to acquire the necessary tunability. In addition, two 100 k Ω resistors are placed at the two ends of the bias lines to decouple the radio-frequency waves and bias circuitry. Although other means (e.g., p - i - n diodes and phase shifters) could have been considered for introducing the necessary tunability, a varactor diode is deliberately chosen here because it offers (i) low insertion loss, (ii) continuous tunability, and (iii) consumes nearly negligible power when it is electrically tuned. Specifically, the power consumption is on the order of nanowatts, as *reverse* biased voltages are applied to varactor diodes to tune their capacitances. In particular, the diode we use from MACOM varies its capacitance from 1.2 to 0.22 pF for the reverse bias voltages ranging from 0 to 10 V.

Unlike static meta-atom designs in which various geometrical parameters can be utilized to control the EM responses, one of the challenges in designing a reconfigurable meta-atom is in the limited number of tuning parameters. For example, the resonance frequency of a single-loop meta-atom (whose equivalent circuit model is

a series LC circuit) can be widely tuned by varying the width and height of the loop. However, such a wide tuning range from capacitance to inductance can be difficult to achieve if it is electronically tuned with just one varactor diode. Moreover, with only one tuning parameter, it is also challenging to ensure a smooth variation to avoid any sensitivity issues. Indeed, previously reported tunable admittance surfaces have shown limited admittance tunability. For example, a meta-atom reported in [63] also utilizes one varactor diode to tune the surface reactance, but its tunability merely ranges from -40 to 0 Ω at 5 GHz. Although it is possible to consider adding more varactor diodes to increase the number of tuning parameters, this would further complicate the required biasing, and it is therefore avoided. Instead, we add an extra loop in the single-loop structure to increase the degrees of freedom in optimizing the geometrical parameters. In particular, while assuming that the diode is biased at 5 V, the geometrical parameters shown in Fig. 7(b) are optimized in ANSYS HIGH FREQUENCY STRUCTURE SIMULATOR (HFSS) to place the meta-atom near its resonance such that the change in voltage can result in a wide and smooth variation of the impedance values from inductance to capacitance. In the simulation, a periodic boundary condition and Floquet port excitations have been used to simulate an array of the meta-atoms, and the angle of incidence is set to 54° instead of 0° to model the guided mode. On the other hand, to model the diode, a separate circuit simulation in ADVANCED DESIGN SYSTEM (ADS) is performed to extract the resistance and capacitance values of the diode as a function of the applied bias voltages. This data is then exported to the HFSS simulation in which the diodes are modeled as lumped RLC boundaries. Table I summarizes the optimized geometrical parameters from the HFSS simulation, and Figs. 8(a) and 8(b) show the scattering properties of the meta-atom array and its variation in the surface reactance values, $\text{Im}[Z_{MA}]$, respectively, as a function of the bias voltages. It should be noted that Fig. 8(a) shows the scattering properties of one layer of the meta-atom array and the proposed HMS consists of three layers of this array for synthesizing the required reflection and transmission properties. In particular, it is seen from Fig. 8(b) that $\text{Im}[Z_{MA}]$ widely and smoothly varies from inductance (600 Ω) to capacitance (-320 Ω), whereas the surface resistance, $\text{Re}[Z_{MA}]$, remains below 40 Ω for all voltages. Based on this one-to-one relationship between the bias voltages and the surface reactance values, the required bias voltages on each layer are obtained. Specifically, Figs. 8(c)

TABLE I. The geometrical parameters of the dual-loop meta-atom.

A	B	b_1	b_2	g	w
7 mm	4 mm	1 mm	2.5 mm	0.228 mm	0.5 mm

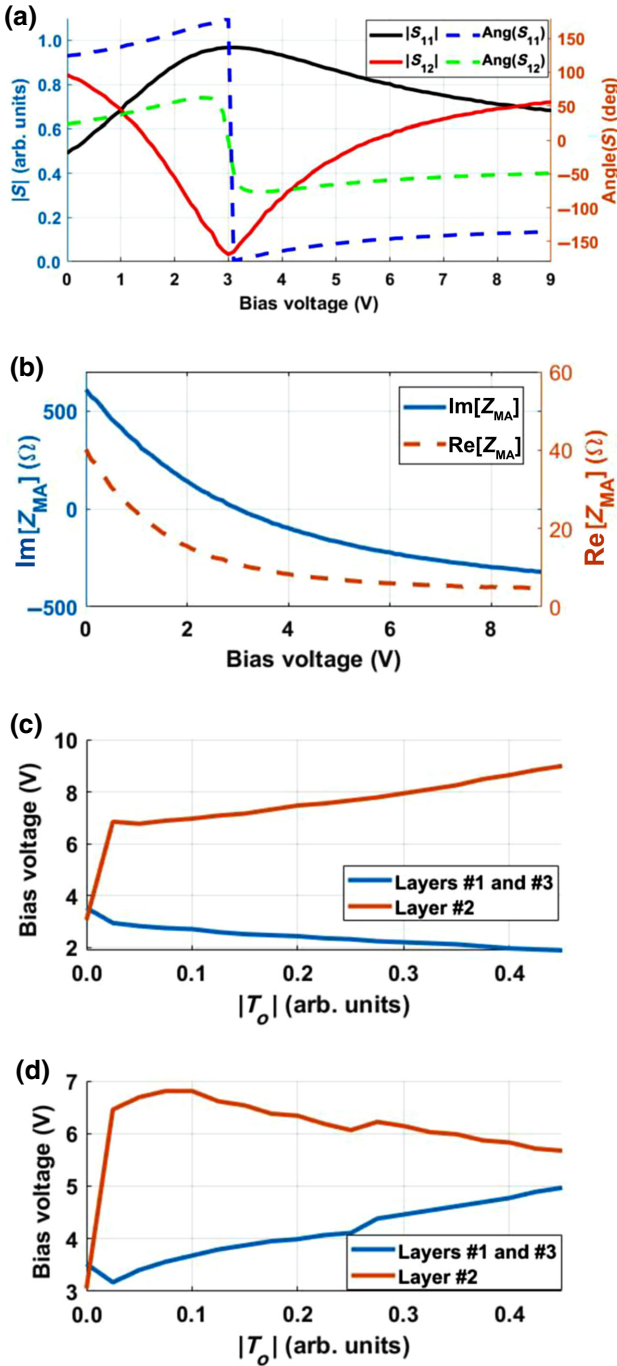


FIG. 8. (a) The scattering properties of the proposed meta atoms and (b) the corresponding surface impedance variation results as a function of the applied bias voltage. The required bias voltages for tuning T_o from 0 to 0.45 with a transmission phase of (c) $+90^\circ$ and (d) -90° .

and 8(d) show the required bias voltages on each layer for synthesizing any values of T_o within the range of $\pm j0.45$, while maintaining the reflection phase of 180° . Although it is possible to further optimize the meta-atom design to increase the range, we have limited the maximum $|T_o|$

to be 0.45 in order to ensure sufficient reflections for the guided mode. In the following full-wave and experimental demonstrations, we use this voltage mapping to physically synthesize the desired scattering parameters in (6) and (7).

On the other hand, to also integrate and cascade the proposed meta-atom arrays within a wave-guiding structure, we have defined three slots along the inner waveguide walls to insert the arrays to the slots as shown in Fig. 9. Specifically, the slots are defined by etching the inner waveguide walls by 1.575 mm in height (to match the thickness of the Rogers 5880 substrates) and 3 mm in depth. As such, the effective dimension of the meta-atom array inside the proposed waveguide structure is 18 mm \times 15N mm (where N represents the number of meta-atoms) instead of 26 mm \times 15N mm. In the HFSS simulation, this effective dimension is used by setting the size of the periodic boundaries to 18 mm \times 15 mm. On the other hand, to bias each meta-atom from outside, small circular windows having a diameter of 2 mm are defined along the waveguide walls as shown in Figs. 9(a) and 9(b). These holes are etched such that the center of the holes would align to that of the meta-atom as shown in Fig. 9(c). In addition, in integrating the meta-atom arrays, the uppermost layer is flipped to preserve the symmetricity for our nonbianisotropic HMS as shown in Fig. 9(a). Finally, to also integrate a source of excitation within the waveguide, a commercially available SMA connector from Fairview Microwave (SC3029) has also been mounted on the waveguide as shown in Figs. 9(a) and 9(b). In what follows, we utilize this construction of the waveguide to verify the proposed theory and the meta-atom design via full-wave simulations.

B. Full-wave verification

To verify the proposed theory and the meta-atom design, the whole waveguide structure shown in Fig. 9 is simulated via CST Microwave Studio. In particular, the first part of this full-wave verification focuses on the beam steering capability of the proposed waveguide for $-40^\circ \leq \theta_{\text{out}} \leq +40^\circ$ at a fixed T_o of 0.3. For this purpose, the required bias voltages for the digital bits of “−0.3” and “+0.3” are first extracted from the voltage-impedance relation that is established in the meta-atom simulation [Fig. 8(b)]. The distribution of these digital bits is then determined based on the desired S_{21} in (6), and it is further optimized by the value of Φ_{th} from CST simulations. In the simulation, the whole waveguide is excited by a waveport at the input of the SMA connector, and all the Ohmic losses (e.g., metallic, dielectric, and diode losses) are included. The length of the waveguide is set to 7λ , which corresponds to 28 meta-atoms per admittance layer. In addition, the diodes are again modeled as lumped elements whose resistance and capacitance values are imported from the separate ADS simulations.

Figure 10 summarizes the utilized voltage distributions for steering a beam from -40° to $+40^\circ$, and Fig. 11 shows the corresponding far-field radiation patterns. As shown in Fig. 10, the required bias voltages for realizing the two digital bits of “ -0.3 ” and “ $+0.3$ ” are the same in all cases, but their distribution is altered to control the radiation angle similar to period-reconfigurable metasurfaces [42,43]. On the other hand, Fig. 11 shows that the distinct main beams are indeed produced based on the proposed physical structure at the prescribed radiation angles of -40° , -20° , 0° , $+20^\circ$, and $+40^\circ$. In the Supplemental Material, analyses pertaining to the angular resolution and scanning range of the proposed LWA are discussed [64]. As another illustration, Fig. 12 shows the field profiles at a selected few radiation angles. Here, it is clearly seen that a guided mode, which closely resembles a TE_{10} mode, is properly excited, and the desired radiations are observed at -40° , 0° , and $+40^\circ$. Moreover, it is also seen that much of the incident power still remains near the end of the waveguide, which indicates that the waveguide can be made longer than 7λ for higher realized gain values. Nevertheless, we have limited our simulation to a 7λ -long waveguide owing to computational limitations. It should be further noted that the location of the SMA input port has also been optimized

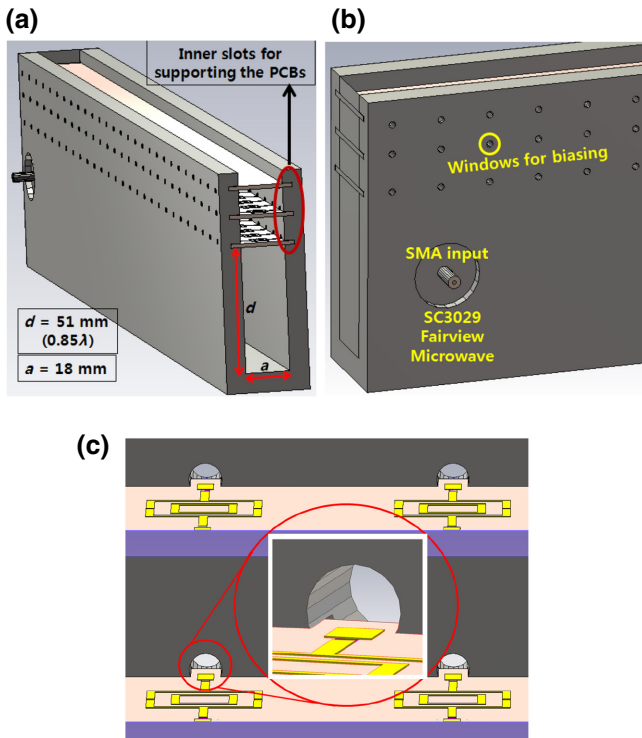


FIG. 9. (a) Overview of the proposed waveguide structure with the tunable admittance layers inserted to the inner slots. (b) Side view of the waveguide showing the location of the SMA input and 2-mm holes that provide an access to the bias lines of the meta-atoms. (c) An internal view of the waveguide.

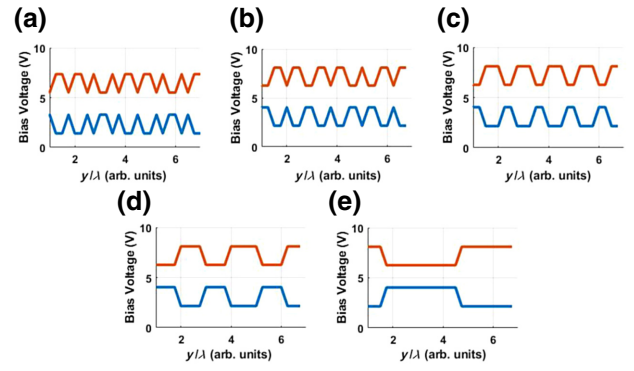


FIG. 10. The digital voltage distributions along the tunable admittance layers at various radiation angles. The orange curve represents the distribution in the first and the third layers, whereas the blue curve represents that in the middle layer for (a) $\theta_{\text{out}} = -40^\circ$, (b) $\theta_{\text{out}} = -20^\circ$, (c) $\theta_{\text{out}} = 0^\circ$, (d) $\theta_{\text{out}} = 20^\circ$, and (e) $\theta_{\text{out}} = 40^\circ$.

to ensure that most of the input power is transferred to the guided mode and the desired radiation. Specifically, Table II summarizes the simulated reflections from the SMA port at various scan angles as well as the simulated losses. As indicated, the input reflections from the SMA port are well below -10 dB for all radiation angles, which also indicates that the open-stopband effect is successfully suppressed in steering a beam.

In addition to the beam steering, the proposed waveguide can also independently manipulate the amplitude of the radiated field by controlling T_o . To demonstrate this point, we consider a simple case in which the HMS is biased to radiate at broadside, however, with $T_o = 0.3$ and $T_o = 0.45$. Although T_o may take a nonuniform form, this example fully demonstrates functionality that cannot be realized with conventional tunable metasurfaces that do

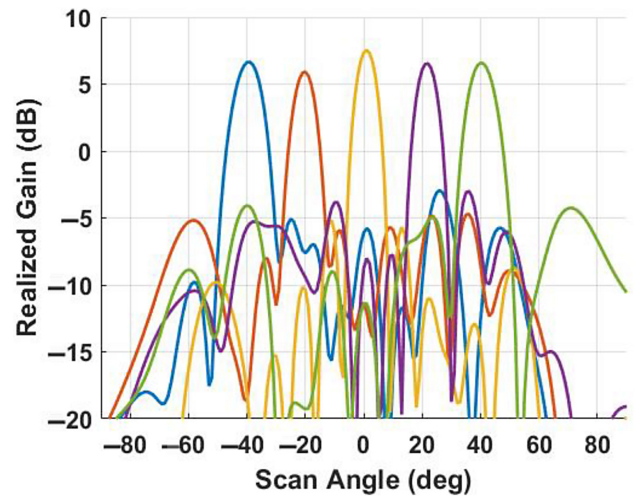


FIG. 11. Full-wave radiation patterns (gains) at various radiation angles for $T_o = 0.3$.

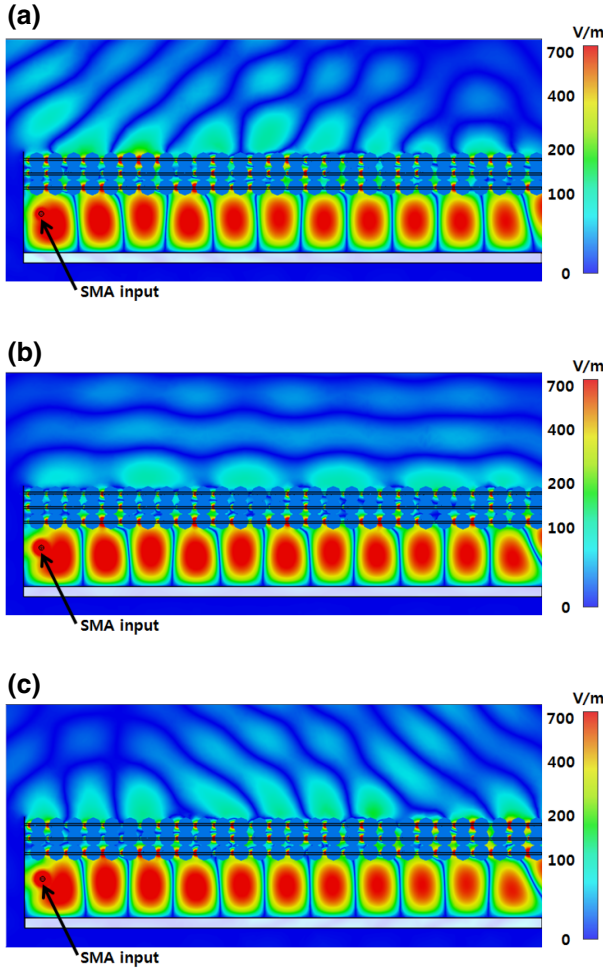


FIG. 12. The field profiles of the simulated waveguide for (a) $\theta_{\text{out}} = -40^\circ$, (b) $\theta_{\text{out}} = 0^\circ$, and (c) $\theta_{\text{out}} = +40^\circ$ for $T_o = 0.3$.

not have any means of amplitude control. The required voltage distribution for $T_o = 0.3$ at broadside is shown in 10(c). For $T_o = 0.45$, the same distribution of the digital bits is used, but the bias voltage values are correspondingly updated to synthesize the new digital values of -0.45

TABLE II. The simulated reflections from the SMA input, the overall loss of the 7λ -long waveguide, and the overall radiation efficiency of the proposed antenna at various scan angles.

θ_{out}	Reflection from the SMA input	Simulated loss (7λ -long waveguide)	Radiation efficiency
-40°	-17.6 dB	3.4 dB	46%
-20°	-15.6 dB	3.9 dB	40.5%
0°	-21.2 dB	3.3 dB	47%
20°	-17.6 dB	3.9 dB	40.2%
40°	-24.2 dB	3.4 dB	45.7%

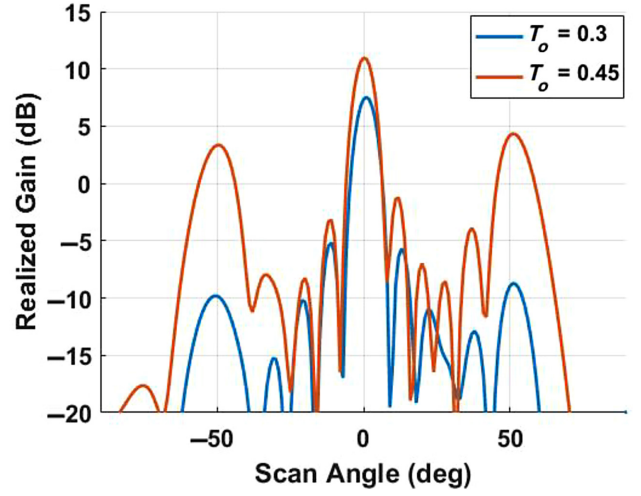


FIG. 13. Full-wave radiation patterns for two broadside radiations with different amplitudes.

and $+0.45$. Figure 13 shows the resulting far-field radiation patterns from CST simulations in which it is clearly seen that the realized gain is increased from 7.3 to 11 dB. Such an increase also closely matches the previous antenna-array analysis in which an increase of approximately 3.5 dB is estimated by increasing T_o from 0.3 to 0.45 [Fig. 6(c)]. However, although Fig. 13 indicates that the amplitude of the main beam is indeed increased, it is also seen that the unwanted sidelobes at $\pm 50^\circ$ are correspondingly increased. This can be attributed to the fact that the guided mode further deviates from an ideal TE_{10} mode as T_o approaches to unity. In particular, it is reiterated that the reflection profile of the HMS, which governs a guided mode, is directly related to T_o through the local power conservation condition [see (7)]. As such, when increasing T_o , the reflection magnitude correspondingly decreases and the phase constant of a guided mode would further deviate from that of a TE_{10} mode. This implies that the value of T_o should be limited. However, this is indeed desirable in our case for the guided-wave-excited HMS as a guided mode must sufficiently propagate to illuminate the entire surface.

IV. EXPERIMENTAL VERIFICATION

To further verify the proposed idea of dynamic and independent control of the radiation angle and the amplitude, we have fabricated the proposed guided-wave-excited HMS as shown in Fig. 14. In particular, Fig. 14(a) shows the fabricated waveguide structure that can be split into half. Here, the inner waveguide walls have been etched to realize the three slots such that each admittance layer can be inserted to one of the halves as shown in Fig. 14(b). In fabricating the tunable admittance layers, we have deliberately avoided using a wave soldering machine for assembling the circuit components as applying a sequence of

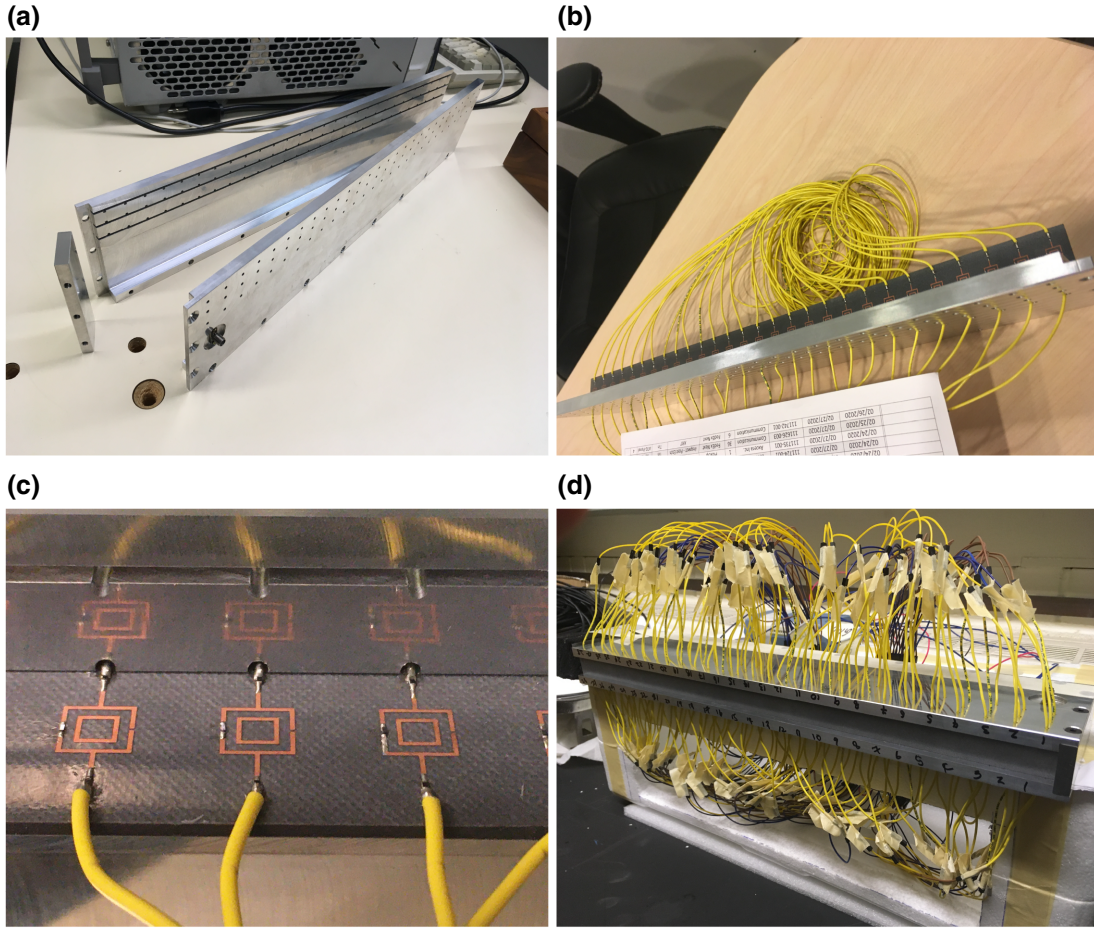


FIG. 14. (a) The fabricated wave-guiding structure in which three slots are defined along the waveguide walls, (b),(c) the integration of the fabricated tunable admittance layers with the waveguide, and (d) the assembled guided-wave-excited reconfigurable HMS.

high temperatures to Rogers 5880 substrates can appreciably shrink their sizes. Such a shrinkage is highly undesirable because it can alter the EM responses, and also cause a misalignment between the centers of the meta-atoms and the holes along the waveguide walls. As such, the resistors, diodes, and wires have all been manually soldered for all of the meta-atoms. Indeed, Fig. 14(c) shows that the centers of the holes and the meta-atoms are well aligned. Once all the tunable admittance layers are inserted to one of the halves, the other half of the waveguide is then put together to result in the final form as shown in Fig. 14(d). As the end of the waveguide is left open, we place an absorber at the end to avoid an open-ended waveguide radiation.

On the other hand, to apply the necessary bias voltages to individual meta-atoms, we have employed a variable voltage source from Measurement Computing (Model No.: USB-3114). This voltage source has 16 output channels each capable of providing a voltage from 0 to 10 V. Although 16 output channels may seem insufficient to control all 84 meta-atoms in the fabricated sample, 4 output

channels are sufficient as a result of the symmetry in our nonbianisotropic HMS and the proposed digital sampling method. Specifically, the first channel of the voltage source is assigned to output the required bias voltage for synthesizing a digital bit of “ $-T_o$ ” for the meta-atoms located on the first and the third layers. On the other hand, the second channel is allocated to output the bias voltage for the “ $+T_o$ ” bits for the meta-atoms on the first and the third layers. Similarly, the third and the fourth channels are respectively assigned to output the required voltages for the “ $-T_o$ ” and “ $+T_o$ ” bits for the meta-atoms in the middle layer. Then, to properly distribute these voltages along the HMS for a certain desired radiation angle, we have used a breadboard to group the meta-atoms that share the same bias voltage. By electrically connecting these groups to the corresponding output channels, we have assigned the required bias voltages to all 84 meta-atoms. This method, however, requires a manual rerouting of the wires on the breadboard to change the voltage distribution for different radiation angles. Nevertheless, a programmable circuit can be devised in the future to automate this process.

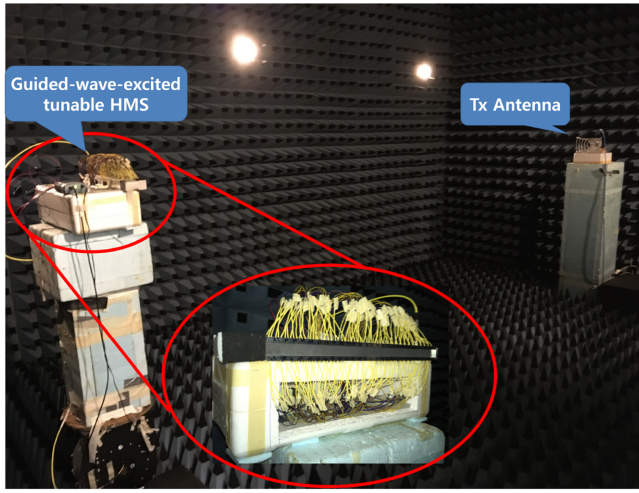


FIG. 15. Far-field anechoic chamber radiation pattern measurement setup.

With the assembled guided-wave-excited reconfigurable HMS, we have performed far-field anechoic chamber measurements to first characterize its beam-steering capability. Figure 15 shows the experimental setup. In this setup, a transmitting horn antenna is placed sufficiently far from

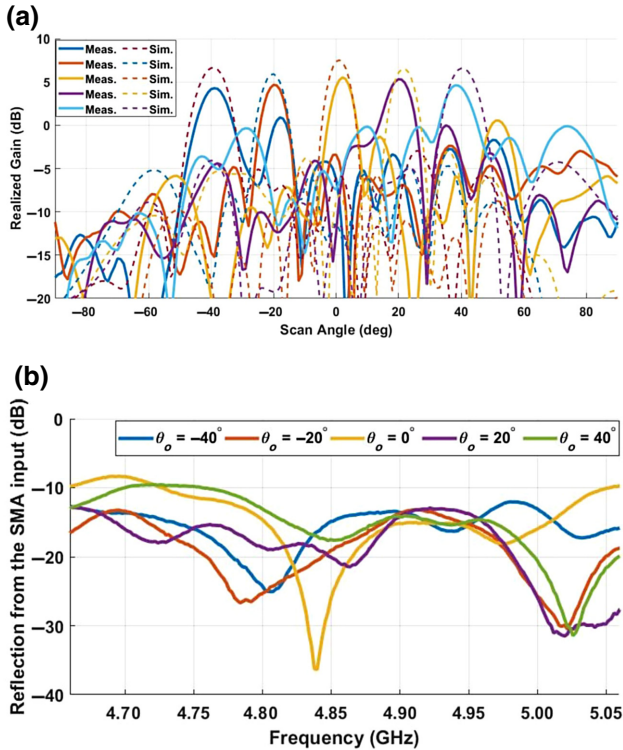


FIG. 16. (a) The measured far-field radiation pattern of the fabricated guided-wave-excited HMS at 4.86 GHz (solid) and the simulated patterns at 5 GHz (dotted). (b) The measured reflections from the SMA port of the waveguide for various steering angles.

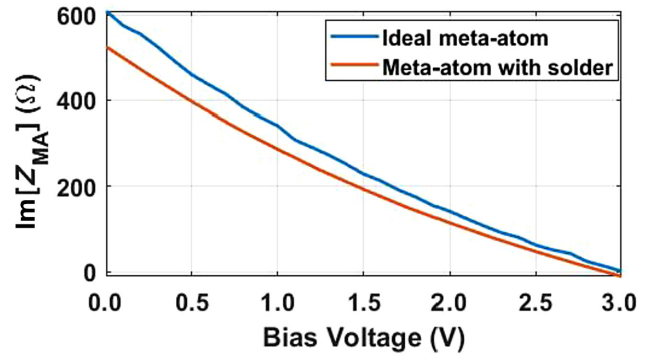


FIG. 17. The influence of excessive solders on the surface reactance values.

the assembled HMS to produce a planar wavefront. On the other hand, the assembled HMS acts as a receiving antenna, and it is placed on a rotational stage. In each measurement, the bias voltages have been fixed to direct a beam at a particular radiation angle, θ_{out} , and the HMS is rotated from -90° to $+90^\circ$ to verify whether the beam is indeed produced at θ_{out} . Specifically, to make a direct comparison with the simulated patterns in Fig. 11, the simulated voltages shown in Fig. 10 are used to bias the meta-atoms. In addition, we have also allowed the simulated voltages to vary within $\pm 15\%$ to account for the influence of fabrication imperfections. Figure 16(a) summarizes the measured radiation patterns at the frequency of 4.86 GHz, which is close to the designed operating frequency of 5 GHz. As shown, the distinct main beams are produced and steered to the prescribed radiation angles. These main beams also closely match to those from the simulated results. However, we also see an increase in the sidelobe levels, which can be contributed to fabrication imperfections. Specifically, these fabrication imperfections mainly originate from the manual soldering of active circuit components, which inevitably left an excessive amount of solder on each meta-atom. This can alter the surface impedance values appreciably, especially when trying to synthesize inductive values as shown in Fig. 17. It should be noted that such a variation in the surface impedance values would be different between all the meta-atoms as the amounts of excessive solder would be different from one to another. On the other hand, it should be reiterated that, in our current case, all the meta-atoms that share the same bias voltages are grouped together on the breadboard. As such, although the simulated voltages have been varied to counter the influence of fabrication imperfections, a degradation in the measured radiation patterns is inevitable. Moreover, a further degradation can be caused from over- or under-etching the metallic patterns, which results in shifting the operating frequency. Despite these issues, however, Fig. 16(a) shows that the assembled HMS can electronically steer a distinct main beam

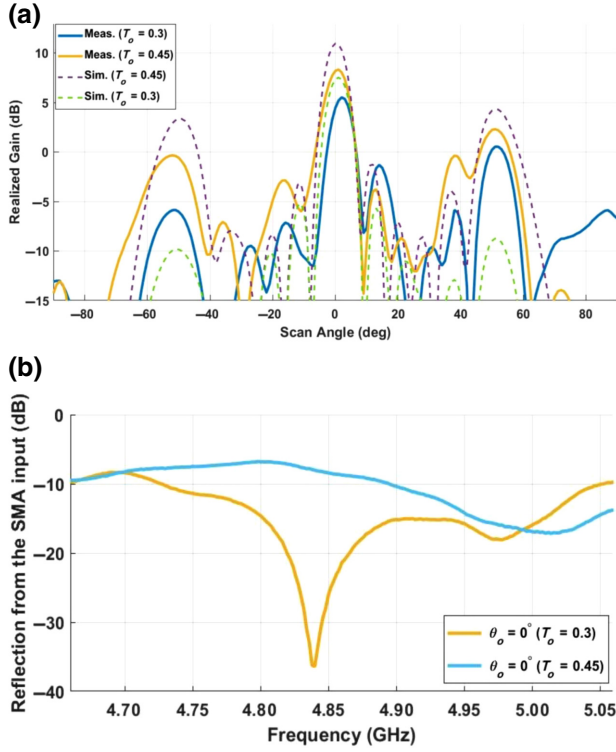


FIG. 18. (a) Far-field anechoic chamber radiation pattern measurement results for two broadside radiation at $T_o = 0.3$ and $T_o = 0.45$ at 4.86 GHz (solid) and the simulated patterns at 5 GHz (dotted) and (b) the measured reflections from the SMA port of the waveguide for two broadside radiation at $T_o = 0.3$ and $T_o = 0.45$.

from -40° to $+40^\circ$. Compared with the simulated realized gains, however, the maximum difference in the measured peak realized gain is approximately 2.5 dB. Such a difference is attributed to inaccurate modeling of the actual Ohmic losses and fabrication errors. Specifically, in our simulations, the active circuit components are modeled as ideal lumped RLC ports without any excessive amounts of solder around them. As discussed previously, excessive solder could have a considerable effect on the surface impedance values, which indeed shifted our operating frequency from 5 to 4.86 GHz. At lower operating frequencies, the effective aperture also accordingly decreases which reduces the gain value. As such, the difference in the simulated and actual Ohmic losses, in addition to the fabrication imperfections, contributed to the difference in the gain values.

To also demonstrate that the assembled waveguide structure successfully suppresses the open-stopband effect for all of the demonstrated steering angles, we have also measured the reflections from the SMA input of the waveguide. In particular, Fig. 16(b) shows the reflection measurement results when our tunable HMS is biased to radiate

from -40° to $+40^\circ$. Similar to the CST simulation, the measured reflections from the SMA port are all below -10 dB near the frequency of 4.86 GHz for all the scan angles, which indicates that the input power is mostly transmitted to the guided mode and then it is radiated out.

Finally, to also confirm the amplitude tunability of the fabricated HMS, we have conducted another measurement for broadside radiation at $T_o = 0.45$ to directly compare the measured results with the simulated ones in Fig. 13. Figure 18(a) shows the comparison between the measured and simulated radiation patterns. Here, it is clearly seen that the measured realized gain is increased by 2.97 dB by increasing T_o from 0.3 to 0.45. Such an increase also closely matches the prediction from the simulation in which an increase of 3.7 dB is observed. As such, despite obvious fabrication imperfections, the far-field anechoic chamber measurement results confirm that the assembled waveguide indeed dynamically and independently controls the direction of the radiated field and the amplitude of the field.

V. CONCLUSION

We propose a guided-wave-excited tunable HMS that offers dynamic and independent control over the angular direction and the amplitude of the radiated field (gain) in the microwave regime. We achieve this by cascading three tunable admittance layers to form the metasurface in which each layer is suitably biased to synthesize particular surface admittance profiles. By dynamically tuning these profiles, the reflection and transmission properties of the metasurface are dynamically and independently controlled to (i) support a guided mode and (ii) transform the guided mode into an aperture field that propagates to a desired radiation. In particular, to also control the amplitude of the radiated field, the aperture field is synthesized with two digital bits of “ $-|T_o|$ ” and “ $+|T_o|$,” where T_o represents the user-defined local transmission amplitude of the metasurface. The metasurface is fabricated based on varactor-diode-loaded dual-loop meta-atoms, and it is also integrated with a specially-designed waveguide. As a proof of concept, we experimentally show dynamic beam steering from -40° to $+40^\circ$, and two broadside radiations with different radiation amplitudes from far-field anechoic chamber measurements. It should also be pointed out that the proposed approach consumes very little dc power (of the order of nanowatts) because the varactor diodes are reverse biased. All these attributes pave the way for an advanced generation of scanning antennas for emerging applications in 5G and 6G telecommunications, radar systems for autonomous vehicles, traffic control, etc.

ACKNOWLEDGMENT

The authors would like to thank Mr. Chang-Soo Kim and Mr. Si-Won Kim from Alpha Precision Co. for their

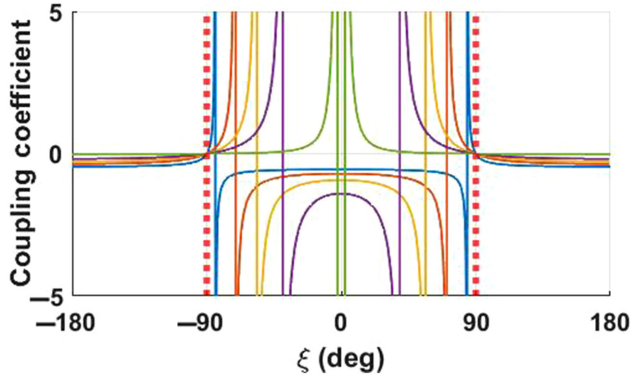


FIG. 19. The magnetolectric coupling coefficient as a function of ξ . The curves with different color represent different T_o .

support in the design and fabrication of the waveguide used in this work. We also would like to thank Rogers for providing Rogers 5880 substrate samples.

APPENDIX A: PASSIVITY AND LOSSLESSNESS OF THE PROPOSED NONBIANISOTROPIC HUYGENS' METASURFACE

Here, we show that the proposed nonbianisotropic HMS indeed satisfies the passivity and losslessness conditions for the desired scattering parameters in (6) and (7) for arbitrary T_o and $\xi = \pm 90^\circ$. For this purpose, we invoke the bianisotropic boundary conditions (with the reciprocity condition applied), and show that the magnetolectric coupling coefficient, K_{em} , is zero. Specifically, the bianisotropic boundary conditions are given as

$$\begin{aligned} & \frac{1}{2} (\vec{E}_{inc} + \vec{E}_{ref} + \vec{E}_{trans}) \\ &= Z_{se} \left\{ \vec{a}_z \times [\vec{H}_{trans} - (\vec{H}_{inc} + \vec{H}_{ref})] \right\} \\ &- K_{em} \left(\vec{a}_z \times \left\{ -\vec{a}_z \times [\vec{E}_{trans} - (\vec{E}_{inc} + \vec{E}_{ref})] \right\} \right) \end{aligned} \quad (A1a)$$

$$\begin{aligned} & \frac{1}{2} (\vec{H}_{inc} + \vec{H}_{ref} + \vec{H}_{trans}) \\ &= Y_{sm} \left\{ -\vec{a}_z \times [\vec{E}_{trans} - (\vec{E}_{inc} + \vec{E}_{ref})] \right\} \\ &+ K_{em} \left(\vec{a}_z \times \left\{ \vec{a}_z \times [\vec{H}_{trans} - (\vec{H}_{inc} + \vec{H}_{ref})] \right\} \right). \end{aligned} \quad (A1b)$$

By substituting the local field quantities in (5) to (A1), Z_{se} , Y_{sm} , and K_{em} can be obtained for S_{11} and S_{21} with arbitrary T_o and ξ . In particular, Fig. 19 shows K_{em} as a function of ξ for various T_o . From the figure, it is clearly seen that K_{em} is identically zero for $T_o \in \{0, 1\}$ only when $\xi = \pm 90^\circ$.

- [1] N. Yu, P. Genevet, M. A. Kats, F. Aieta, J. Tetienne, F. Capasso, and Z. Gaburro, Light propagation with phase discontinuities: Generalized laws of reflection and refraction, *Science* **334**, 333 (2011).
- [2] N. Yu, P. Genevet, F. Aieta, M. A. Kats, R. Blanchard, G. Aoust, J. Tetienne, Z. Gaburro, and F. Capasso, Flat optics: Controlling wavefronts with optical antenna metasurfaces, *IEEE J. Sel. Top. Quantum Electron.* **19**, 4700423 (2013).
- [3] X. Ni, N. K. Emani, A. V. Kildishev, A. Boltasseva, and V. M. Shalaev, Broadband light bending with plasmonic nanoantennas, *Science* **335**, 427 (2012).
- [4] F. Monticone, N. M. Estakhri, and A. Alù, Full Control of Nanoscale Optical Transmission with a Composite Metascreen, *Phys. Rev. Lett.* **110**, 203903 (2013).
- [5] C. Pfeiffer and A. Grbic, Metamaterial Huygens' Surfaces: Tailoring Wave Fronts with Reflectionless Sheets, *Phys. Rev. Lett.* **110**, 197401 (2013).
- [6] M. Selvanayagam and G. V. Eleftheriades, Discontinuous electromagnetic fields using orthogonal electric and magnetic currents for wavefront manipulation, *Opt. Express* **21**, 14409 (2013).
- [7] M. Selvanayagam and G. V. Eleftheriades, Experimental Demonstration of Active Electromagnetic Cloaking, *Phys. Rev. X* **3**, 041011 (2013).
- [8] M. Gharghi, C. Gladden, T. Zentgraf, Y. Liu, X. Yin, J. Valentine, and X. Zhang, A carpet cloak for visible light, *Nano Lett.* **11**, 2825 (2011).
- [9] Y. Yang, H. Wang, F. Yu, Z. Xu, and H. Chen, A metasurface carpet cloak for electromagnetic, acoustic and water waves, *Sci. Rep.* **6**, 20219 (2016).
- [10] X. Ni, A. V. Kildishev, and V. M. Shalaev, Metasurface holograms for visible light, *Nat. Commun.* **4**, 1 (2013).
- [11] L. Huang, X. Chen, H. Mühlenbernd, H. Zhang, S. Chen, B. Bai, Q. Tan, G. Jin, K. Cheah, C. Qiu, J. Li, T. Zentgraf, and S. Zhang, Three-dimensional optical holography using a plasmonic metasurface, *Nat. Commun.* **4**, 2808 (2013).
- [12] M. Kim, J. Jeong, J. K. S. Poon, and G. V. Eleftheriades, Vanadium-dioxide-assisted digital optical metasurfaces for dynamic wavefront engineering, *J. Opt. Soc. Am. B* **33**, 980 (2016).
- [13] M. Kim, A. M. H. Wong, and G. V. Eleftheriades, Optical Huygens' Metasurfaces with Independent Control of the Magnitude and Phase of the Local Reflection Coefficients, *Phys. Rev. X* **4**, 041042 (2014).
- [14] A. Epstein and G. V. Eleftheriades, Passive lossless huygens metasurfaces for conversion of arbitrary source field to directive radiation, *IEEE Trans. Antennas Propag.* **62**, 5680 (2014).
- [15] A. Epstein and G. V. Eleftheriades, Synthesis of Passive Lossless Metasurfaces Using Auxiliary Fields for Reflectionless Beam Splitting and Perfect Reflection, *Phys. Rev. Lett.* **117**, 256103 (2016).
- [16] M. Chen, E. Abdo-Sánchez, A. Epstein, and G. V. Eleftheriades, Theory, design, and experimental verification of a reflectionless bianisotropic Huygens' metasurface for wide-angle refraction, *Phys. Rev. B* **97**, 125433 (2018).
- [17] S. Schelkunoff, Some equivalence theorems of electromagnetics and their application to radiation problems, *Bell Syst. Tech. J.* **15**, 92 (1936).

- [18] M. Selvanayagam and G. V. Eleftheriades, Polarization control using tensor Huygens' surfaces, *IEEE Trans. Antennas Propag.* **62**, 6155 (2014).
- [19] M. Kim and G. V. Eleftheriades, Design and Experimental Demonstration of Impedance-Matched Circular-Polarization-Selective Surfaces with Spin-Selective Phase Modulations, *Phys. Rev. Appl.* **13**, 014009 (2020).
- [20] L. Boccia, F. Venneri, G. Amendola, and G. D. Massa, in *IEEE Antennas and Propagation Society International Symposium*, (IEEE, San Antonio, TX, USA, 2002), Vol. 3, p. 132.
- [21] S. V. Hum, M. Okoniewski, and R. J. Davies, Realizing an electronically tunable reflectarray using varactor diode-tuned elements, *IEEE Microw. Wirel. Compon. Lett.* **15**, 422 (2005).
- [22] M. Riel and J. Laurin, Design of an electronically beam scanning reflectarray using aperture-coupled elements, *IEEE Trans. Antennas Propag.* **55**, 1260 (2007).
- [23] S. Tian, Y. Zhao, and L. Li, in *2018 Cross Strait Quad-Regional Radio Science and Wireless Technology Conference (CSQRWC)* (IEEE, Xuzhou, China, 2018), p. 1.
- [24] B. Ratni, A. de Lustrac, G.-P. Piau, and S. N. Burokur, Active metasurface for reconfigurable reflectors, *Appl. Phys. A* **124**, 104 (2018).
- [25] H. Kamoda, T. Iwasaki, J. Tsumochi, and T. Kuki, in *2009 IEEE MTT-S International Microwave Symposium Digest* (IEEE, Boston, MA, USA, 2009), p. 1177.
- [26] E. Carrasco, M. Barba, and J. A. Encinar, X-band reflectarray antenna with switching-beam using PIN diodes and gathered elements, *IEEE Trans. Antennas Propag.* **60**, 5700 (2012).
- [27] Y. Li and A. Abbosh, Reconfigurable reflectarray antenna using single-layer radiator controlled by PIN diodes, *IET Microw. Antennas Propag.* **9**, 664 (2015).
- [28] H. Rajagopalan, Y. Rahmat-Samii, and W. A. Imbriale, RF MEMS actuated reconfigurable reflectarray patch-slot element, *IEEE Trans. Antennas Propag.* **56**, 3689 (2008).
- [29] A. Munoz-Acevedo, P. Padilla, and M. Sierra-Castaner, in *2009 3rd European Conference on Antennas and Propagation* (IEEE, Berlin, Germany, 2009), p. 1201.
- [30] L. Boccia, I. Russo, G. Amendola, and G. D. Massa, Multilayer antenna-filter antenna for beam-steering transmitarray applications, *IEEE Trans. Microw. Theory Tech.* **60**, 2287 (2012).
- [31] J. Y. Lau and S. V. Hum, A wideband reconfigurable transmitarray element, *IEEE Trans. Antennas Propag.* **60**, 1303 (2012).
- [32] J. Y. Lau and S. V. Hum, Reconfigurable transmitarray design approaches for beamforming applications, *IEEE Trans. Antennas Propag.* **60**, 5679 (2012).
- [33] C. Cheng and A. Abbaspour-Tamijani, Study of 2-bit antenna-filter-antenna elements for reconfigurable millimeter-wave lens arrays, *IEEE Trans. Microw. Theory Tech.* **54**, 4498 (2006).
- [34] A. Clemente, L. Dussopt, R. Sauleau, P. Potier, and P. Pouliguen, 1-bit reconfigurable unit cell based on pin diodes for transmit-array applications in X-band, *IEEE Trans. Antennas Propag.* **60**, 2260 (2012).
- [35] L. D. Palma, A. Clemente, L. Dussopt, R. Sauleau, P. Potier, and P. Pouliguen, in *2015 9th European Conference on Antennas and Propagation (EuCAP)* (IEEE, Hiroshima, Japan, 2015), p. 1.
- [36] L. D. Palma, A. Clemente, L. Dussopt, R. Sauleau, P. Potier, and P. Pouliguen, 1-bit reconfigurable unit cell for Ka-band transmitarrays, *IEEE Antennas Wirel. Propag. Lett.* **15**, 560 (2016).
- [37] D. Sievenpiper, J. Schaffner, B. Loo, G. Tangonan, R. Harold, J. Pikulski, and R. Garcia, in *Antennas and Propagation Society International Symposium, 2001* (IEEE, Boston, MA, USA, 2001), Vol. 1, p. 174, <https://doi.org/10.1109/APS.2001.958820>.
- [38] D. Sievenpiper and J. Schaffner, Beam steering microwave reflector based on electrically tunable impedance surface, *Electron. Lett.* **38**, 1237 (2002).
- [39] T. Hand and S. Cummer, Reconfigurable reflectarray using addressable metamaterials, *Antennas Wireless Propag. Lett., IEEE* **9**, 70 (2010).
- [40] Z. Wei, Y. Cao, X. Su, Z. Gong, Y. Long, and H. Li, Highly efficient beam steering with a transparent metasurface, *Opt. Express* **21**, 10739 (2013).
- [41] B. O. Zhu, J. Zhao, and Y. Feng, Active impedance metasurface with full 360° reflection phase tuning, *Sci. Rep.* **3**, 3059 (2013).
- [42] D. K. Karmokar, D. N. P. Thalakituna, K. P. Esselle, M. Heimlich, and L. Matekovits, in *2013 International Symposium on Electromagnetic Theory* (2013), p. 436.
- [43] Z. Li, Y. J. Guo, S. Chen, and J. Wang, A period-reconfigurable leaky-wave antenna with fixed-frequency and wide-angle beam scanning, *IEEE Trans. Antennas Propag.* **67**, 3720 (2019).
- [44] A. Suntives and S. V. Hum, A fixed-frequency beam-steerable half-mode substrate integrated waveguide leaky-wave antenna, *IEEE Trans. Antennas Propag.* **60**, 2540 (2012).
- [45] M. Wang, H. F. Ma, H. C. Zhang, W. X. Tang, X. R. Zhang, and T. J. Cui, Frequency-fixed beam-scanning leaky-wave antenna using electronically controllable corrugated microstrip line, *IEEE Trans. Antennas Propag.* **66**, 4449 (2018).
- [46] C. Damm, M. Maasch, R. Gonzalo, and R. Jakob, in *2010 IEEE MTT-S International Microwave Symposium* (IEEE, Anaheim, CA, USA, 2010), p. 13.
- [47] E. Abdo-Sánchez, A. Epstein, and G. V. Eleftheriades, Reconfigurability mechanisms with scanning rate control for omega-bianisotropic Huygens' metasurface leaky-wave antennas, *IEEE Access* **7**, 168247 (2019).
- [48] J. G. Nicholls and S. V. Hum, Full-space electronic beam-steering transmitarray with integrated leaky-wave feed, *IEEE Trans. Antennas Propag.* **64**, 3410 (2016).
- [49] A. H. Dorrah and G. V. Eleftheriades, Bianisotropic huygens' metasurface pairs for nonlocal power-conserving wave transformations, *IEEE Antennas Wirel. Propag. Lett.* **17**, 1788 (2018).
- [50] B. O. Raeker and A. Grbic, Compound Metaoptics for Amplitude and Phase Control of Wave Fronts, *Phys. Rev. Lett.* **122**, 113901 (2019).
- [51] K. Chen, Y. Feng, F. Monticone, J. Zhao, B. Zhu, T. Jiang, L. Zhang, Y. Kim, X. Ding, S. Zhang, A. Alù, and C.-W. Qiu, A reconfigurable active Huygens' metalens, *Adv. Mater.* **29**, 1606422 (2017).

- [52] M. Y. Xu and S. V. Hum, in *2019 13th European Conference on Antennas and Propagation (EuCAP)* (IEEE, Krakow, Poland, 2019), p. 1.
- [53] M. Kim and G. V. Eleftheriades, in *2020 14th European Conference on Antennas and Propagation (EuCAP)* (2020), p. 1.
- [54] M. Kim and G. V. Eleftheriades, in *2020 Fourteenth International Congress on Artificial Materials for Novel Wave Phenomena (Metamaterials)* (2020), (to be published).
- [55] J. Wong, M. Selvanayagam, and G. V. Eleftheriades, in *IEEE International Microwave Symposium* (IEEE, Baltimore, USA, 2011).
- [56] E. Abdo-Sánchez, M. Chen, A. Epstein, and G. V. Eleftheriades, A leaky-wave antenna with controlled radiation using a bianisotropic Huygens' metasurface, *IEEE Trans. Antennas Propag.* **67**, 108 (2019).
- [57] E. F. Kuester, M. A. Mohamed, M. Piket-May, and C. L. Holloway, Averaged transition conditions for electromagnetic fields at a metafilm, *IEEE Trans. Antennas Propag.* **51**, 2641 (2003).
- [58] C. L. Holloway, M. A. Mohamed, E. F. Kuester, and A. Dienstfrey, Reflection and transmission properties of a metafilm: With an application to controllable surface composed of resonant particles, *IEEE Trans. Electromagn. Compat.* **47**, 853 (2005).
- [59] J. P. S. Wong, A. Epstein, and G. V. Eleftheriades, Reflectionless wide-angle refracting metasurfaces, *IEEE Antennas Wirel. Propag. Lett.* **15**, 1293 (2016).
- [60] M. Selvanayagam and G. V. Eleftheriades, Circuit modeling of Huygens' surfaces, *IEEE Antennas Wirel. Propag. Lett.* **12**, 1642 (2013).
- [61] T. F. O. Yurduseven, D. Marks, and D. Smith, Dynamically reconfigurable holographic metasurface aperture for a mills-cross monochromatic microwave camera, *Opt. Express* **26**, 5281 (2018).
- [62] X. F. Luo, P. T. Teo, A. Qing, and C. K. Lee, in *ICMMT 4th International Conference on, Proceedings Microwave and Millimeter Wave Technology, 2004* (2004), p. 94.
- [63] S. Liu, H.-X. Xu, H. C. Zhang, and T. J. Cui, Tunable ultrathin mantle cloak via varactor-diode-loaded metasurface, *Opt. Express* **22**, 13403 (2014).
- [64] See Supplemental Material at <http://link.aps.org/supplemental/10.1103/PhysRevApplied.15.054037> for analyses related to the angular resolution and scanning range of the proposed LWA.